



Title	Charge-transport in tin-iodide perovskite CH ₃ NH ₃ SnI ₃ : origin of high conductivity
Author(s)	Takahashi, Yukari; Obara, Rena; Lin, Zheng-Zhong; Takahashi, Yukihiro; Naito, Toshio; Inabe, Tamotsu; Ishibashi, Shoji; Terakura, Kiyoyuki
Citation	Dalton Transactions, 40(20), 5563-5568 https://doi.org/10.1039/c0dt01601b
Issue Date	2011-05-28
Doc URL	http://hdl.handle.net/2115/48597
Rights	Dalton Trans., 2011, 40, 5563-5568 - Reproduced by permission of The Royal Society of Chemistry (RSC)
Type	article (author version)
File Information	DT40-20_5563-5568.pdf



[Instructions for use](#)

Charge-Transport in Tin-Iodide Perovskite $\text{CH}_3\text{NH}_3\text{SnI}_3$: Origin of High Conductivity†

Yukari Takahashi,^a Rena Obara,^{a,d} Zheng-Zhong Lin,^{a,e} Yukihiro Takahashi,^a
Toshio Naito,^a Tamotsu Inabe,^{a,*} Shoji Ishibashi,^b and Kiyoyuki Terakura^{c,f}

^a*Department of Chemistry, Graduate School of Science, Hokkaido University, Sapporo 060-0810, Japan. E-mail: inabe@sci.hokudai.ac.jp*

^b*Nanosystem Research Institute "RICS", National Institute for Advanced Industrial Science and Technology, Tsukuba 305-8568, Japan*

^c*Division of Frontier Research, Creative Research Initiative "Sousei", Hokkaido University, Sapporo 001-0021, Japan*

^d*Present address: Ricoh IT Solutions Co., Ltd. Kitami, Hakuyo-cho, Kitami 090-0013, Japan*

^e*Present address: School of Bioengineering, Jimei University, Xiamen 361021, China*

^f*Present address: Research Center for Integrated Science, Japan Advanced Institute of Science and Technology, 1-1 Asahidai, Nomi, Ishikawa 923-1292, Japan*

†Electronic supplementary information (ESI) Available: Powder diffraction data of $\text{CH}_3\text{NH}_3\text{SnI}_3$ at 150 K and 50 K (1 figure) and crystallographic data in CIF of $\text{CH}_3\text{NH}_3\text{SnI}_3$ at 295 K and 140 K: CCDC reference numbers 801226 and 801227, respectively. DOI: 10.1039/c0dt01601b.

Abstract:

The structural and electrical properties of a metal-halide cubic perovskite, $\text{CH}_3\text{NH}_3\text{SnI}_3$, have been examined. The band structure, obtained using first-principles calculation, reveals a well-defined band gap at the Fermi level. However, the temperature dependence of the single-crystal electrical conductivity shows metallic behavior down to low temperatures. The temperature dependence of the thermoelectric power is also metallic over the whole temperature range, and the large positive value indicates that charge transport occurs with a low concentration of hole carriers. The metallic properties of this as-grown crystal are thus suggested to result from spontaneous hole-doping in the crystallization process, rather than the semi-metal electronic structure. The present study shows that artificial hole doping indeed enhances the conductivity.

Introduction

Perovskites with an $M(1)M(2)X_3$ composition can be constructed with various metal cations ($M(1)$ and $M(2)$) and anions (X), and yield a wide variety of materials, including ferroelectrics, superconductors, ionic conductors, and magnetic conductors. In the case of the conductors, the compounds are exclusively oxides, whereas the halides are insulators in general. The only exception to this is the tin-iodide system, and metallic conductivity of the cubic perovskite of $CH_3NH_3SnI_3$ has been reported.¹ However, recent theoretical band calculations indicated a band gap of 0.46 eV at the Fermi level for this crystal.²

Naively considering the valences of the components ($CH_3NH_3^+$, Sn^{2+} , and Γ^-), there appears to be no source of metallic carriers. Indeed, the analogues of $CH_3NH_3SnCl_3$ and $CH_3NH_3SnBr_3$ are semiconductors with sizable energy gaps; their optically determined band gaps are 3.69 and 2.15 eV, respectively.³ Therefore, the band structure with a band gap seems to be more reasonable for $CH_3NH_3SnI_3$.

For the tin-iodide system, there is another problem that arises from chemical instability. In particular, high contact resistance due to chemical reactions at the interface between the crystal and probes prevents measurements of their intrinsic charge transport properties. Therefore, most measurements so far have been carried out by directly attaching probes to the pressed powder samples.^{1,4-6} Recently, we have developed a method for charge transport measurements for the tin-iodide system.⁷ By employing this method, we examined the charge transport properties of several A_2SnI_4 (A = organic ammonium cation) layered-perovskites, and found that they had rather

high conductivity despite their well-defined band gap greater than 1 eV. Because artificial hole doping enhanced conductivity, charge-transport in the as-grown crystal is considered to be dominated by spontaneous hole doping.⁷

The A_2SnI_4 layered-perovskite is a member of a family of compounds with varying thickness (n) of the perovskite layers, $A_2(CH_3NH_3)_{n-1}Sn_nI_{3n+1}$.^{5,8-13} The cubic perovskite of $CH_3NH_3SnI_3$ is the other side of the end member of this series at $n = \infty$. Therefore, an extrinsic factor might also operate in charge transport in $CH_3NH_3SnI_3$, as observed in A_2SnI_4 . In this paper, we present the preparation of single crystal $CH_3NH_3SnI_3$ as well as its X-ray structure analyses, band structure calculations, electrical conductivity, and thermoelectric power of the as-grown and artificial hole doped crystals, and discuss the origin of the discrepancy between observed and calculated electronic structures.

Experimental Section

Materials

SnI_2 was synthesized by the method reported,¹⁴ and SnI_4 was commercially obtained (Strem Chemicals). Both compounds were purified by vacuum sublimation. CH_3NH_3I was obtained by reaction of aqueous solutions of CH_3NH_2 and HI, and recrystallized by adding ether in the ethanol solution.

Crystal growth

Three methods A, B, and C were used. All the experiments were performed under inert (Ar or N_2) atmosphere.

Method A: Crystals of $\text{CH}_3\text{NH}_3\text{SnI}_3$ were prepared by slow cooling (cooling rate of $2\text{--}3 \text{ K h}^{-1}$, from 75 to $5 \text{ }^\circ\text{C}$) of an aqueous HI solution containing an equimolar mixture of SnI_2 and $\text{CH}_3\text{NH}_3\text{I}$ followed by a method reported by Mitzi.¹ Resulting crystals were relatively small (maximum dimension = 0.3 mm).

Method B: Crystals were prepared by slow cooling (cooling rate of $2\text{--}3 \text{ K h}^{-1}$, from 75 to $5 \text{ }^\circ\text{C}$) of an aqueous HI solution containing SnI_2 and $\text{CH}_3\text{NH}_3\text{I}$ with γ -aminobutyric acid (molar ratio = $1:1:1$). Crystals obtained were elongated in one direction (maximum dimension = 3 mm along the $[1\ 0\ 0]$ direction of the tetragonal phase).

Method C: Anhydrous ethanol was used instead of aqueous HI. Slow cooling (cooling rate of $1\text{--}2 \text{ K h}^{-1}$, from 65 to $5 \text{ }^\circ\text{C}$) of the ethanol solution containing an equimolar mixture of SnI_2 and $\text{CH}_3\text{NH}_3\text{I}$ gave cube-like crystals with relatively large size ($\sim 1 \text{ mm}$).

The crystals obtained from these three methods were harvested by simple filtration, and yielded the same X-ray diffraction data, indicating the same underlying crystal structure.

Artificial doping

Doping was carried out by substituting a part of SnI_2 with SnI_4 in the crystal growth solution. Doped crystals were obtained by slow cooling (cooling rate of $1\text{--}2 \text{ K h}^{-1}$, from 65 to $5 \text{ }^\circ\text{C}$) of the ethanol solution containing a mixture of SnI_2 , SnI_4 , and $\text{CH}_3\text{NH}_3\text{I}$ (molar ratio = $0.8:0.2:1$). The appearance of the crystals was essentially the same as that

of the crystals obtained by method C. There was no detectable difference between the doped and as-grown crystals in X-ray diffraction data. Though the solution contained 20 % of SnI_4 , the doping level of the crystal was much less than the content in the solution, as discussed later.

X-ray structure analyses

Because the crystal surfaces gradually decomposed in air, the freshly prepared crystal samples were coated with an epoxy resin for the measurements at 295 and 140 K. Diffraction data were recorded on a Rigaku R-Axis Rapid imaging plate diffractometer with graphite-monochromated Mo- $K\alpha$ radiation ($\lambda = 0.7107 \text{ \AA}$) equipped with a cold nitrogen gas flow apparatus. The crystal data obtained are summarized in Table 1. The structures were solved using a direct method (SIR-92¹⁵) and refined with all data on F^2 using the CrystalStructure program package.¹⁶ Full-matrix least-squares refinements were performed for tin and iodine atoms with anisotropic thermal parameters. Because site symmetry for CH_3NH_3 was not consistent with the point group of CH_3NH_3 in both structures at 295 and 140 K, the cation must be largely disordered and was not included in the refinement.

Powder diffraction experiments were performed at 150 K and 50 K using a Rigaku Rint 2200 diffractometer with graphite-monochromated Cu- $K\alpha$ radiation ($\lambda = 1.5418 \text{ \AA}$). The sample holder was mounted on the cold head of a displax system with a Be window. In order to minimize the surface degradation, crystals obtained by method A were used without pulverization and coated by grease (Apiezon N).

Table 1 Crystal Data for CH₃NH₃SnI₃

Temperature /K	295	140
Crystal system	cubic	tetragonal
Space group	<i>Pm3m</i>	<i>I4/mcm</i>
<i>a</i> / Å	6.243(1)	8.727(1)
<i>c</i> / Å	–	12.502(2)
<i>V</i> / Å ³	243.4(1)	952.2(2)
<i>Z</i>	1	4
No. of unique reflections	83	291
<i>R</i> ₁ (<i>I</i> > 2.00σ(<i>I</i>))	0.070	0.057
<i>R</i> _w (all data)	0.252	0.268
GOF indicator	1.236	0.914

Resistivity and thermoelectric power measurements

Measurements were performed for crystals obtained by methods B and C. The freshly obtained crystal was mounted on a sample holder, and the sample chamber was immediately evacuated. The temperature dependence was measured in the temperature range of 5–300 K in a dispex system. Electrical contacts between the crystal and gold lead wires ($\phi = 20 \mu\text{m}$ for resistivity measurements) or gold foils (thickness = 1 μm for thermoelectric power measurements) were made using a carbon paste (Dotite). The original thinner (toluene) was evaporated by a stream of N₂ gas, and tetraline (1,2,3,4-tetrahydronaphthalene) was added to the paste as a thinner. The contact resistance was in the range of 100–1000 Ω .⁷ Resistivity was measured by a four-probe method, and thermoelectric power was obtained by a modified method reported by

Chaikin and Kwak.¹⁷

Calculation of electronic structure

Two calculation methods were utilized to obtain the electronic structure. One is an extended Hückel method¹⁸ using the atomic positional parameters of tin and iodine as determined by X-ray structure analysis. We also performed first-principles calculations with our in-house computational code QMAS (Quantum MAterials Simulator¹⁹) adopting the projector augmented-wave method.²⁰ For the exchange and correlation energy for electrons, the PBE version of the generalized gradient approximation (GGA) was used.²¹ In the real system, the CH_3NH_3^+ cation is randomly rotating and the system has cubic symmetry. To mimic this situation, we performed calculations for Cs^+ (cubic symmetry) or fixed CH_3NH_3^+ (reduced symmetry) as the A-site cation with the observed lattice and atomic parameters ($a = 6.243 \text{ \AA}$ for the cubic phase, and $a = 8.727$ and $c = 12.502 \text{ \AA}$ with $x_1 = 0.209$ for the tetragonal phase). We found that band dispersions around the band gap were not affected by this difference in the A-site cation.

Results and discussion

Crystal structures

The analyzed structure based on the diffraction data at 295 K (Fig. 1a) is a cubic perovskite that agrees with the reported structure.¹ This high-temperature structure transforms to a structure with a lower-symmetry at low temperatures. This transition

occurs at around 275 K (as seen from the resistivity measurements), and the crystal system becomes tetragonal as observed for the Pb analogue.^{22,23} As shown in Fig. 1b, the unit lattice of the tetragonal phase corresponds to the $\sqrt{2} \times \sqrt{2} \times 2$ cubic lattice at room temperature. The space group changes from $Pm\bar{3}m$ to $I4/mcm$, with tilting of the SnI_6 octahedrons around the c axis ($a^0a^0c^-$ by the Glazer notation²⁴). Because the symmetry at the CH_3NH_3^+ site is incompatible with the molecular symmetry, the cation is still disordered in this phase. With further lowering of the temperature, a transition with hysteresis was observed at 108–114 K in the resistivity measurements (vide infra). When single-crystal X-ray diffraction experiments were carried out in this temperature regime, a clear structural transition was observed. However, in this transition, the Bragg spots showed inhomogeneous splitting that made impossible to collect the diffraction data. From the powder diffraction data (see ESI Figure S1), the splitting of the single-crystal Bragg spots was found to be due to the symmetry reduction from tetragonal to orthorhombic: the isometric a and b directions in the tetragonal lattice become distinguishable in the orthorhombic lattice and two different orientations of the lattice may occur at the same time. Due to insufficient data quality of the powder diffraction, the space group was not determined. Similar symmetry reduction from tetragonal to orthorhombic was also observed in $\text{CH}_3\text{NH}_3\text{PbI}_3$ below 162.2 K.²⁵

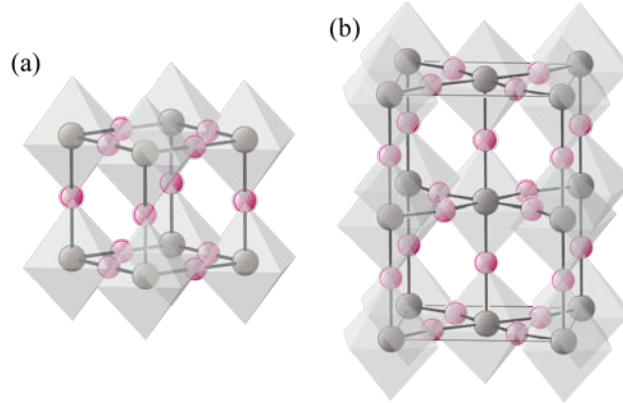


Fig. 1 Crystal structure of $\text{CH}_3\text{NH}_3\text{SnI}_3$ at (a) 295 K and (b) 140 K. Tin is represented by the gray spheres and iodine by the pink spheres. CH_3NH_3 cations are disordered and are not included.

Band structure calculations

In the previous report based on the extended Hückel calculation of $\text{CH}_3\text{NH}_3\text{SnI}_3$, a semi-metal electronic structure was suggested because of a marginal crossing of the valence band and conduction band.^{4,6} In the present study, we also performed the same level calculation. The result obtained from the extended Hückel calculation using the parameters obtained from the structural data at 295 K is shown in Fig. 2a. The top of the valence band (main components: Sn 5s and I 5p) indeed roughly touches to the bottom of the conduction band (main component: Sn 5p) at the R point. On the other hand, a different band structure for $\text{CH}_3\text{NH}_3\text{SnI}_3$ was reported on the basis of more sophisticated first-principles calculations: the band structure has a well-defined band gap at the R point with $E_G = 0.46$ eV.² We also performed the first-principles calculation in which Cs is placed at the A-site instead of CH_3NH_3 to mimic the cubic symmetry, and the band dispersion is shown in Fig. 2c. A direct band gap of 0.37 eV exists at the R point. The obtained band structure of cubic CsSnI_3 is very similar to that reported.²

Subtle differences can be ascribed to the slightly different lattice parameters used. The band structure with a well-defined band gap was also suggested from first-principles calculations for the cubic phase of $\text{CH}_3\text{NH}_3\text{SnI}_3$ ²⁶ and CsSnI_3 .²⁷ It should be noted that the band structures derived from first-principles calculations all have a well-defined band gap. Obviously, the accuracy and reliability of first-principles calculations are higher than those of the extended Hückel calculation. Furthermore, since the band gap is usually underestimated with the first-principles GGA calculation, the above value is thought to specify the lower bound of the gap. Therefore, the electronic structure of cubic $\text{CH}_3\text{NH}_3\text{SnI}_3$ is considered to be a narrow gap semiconductor.

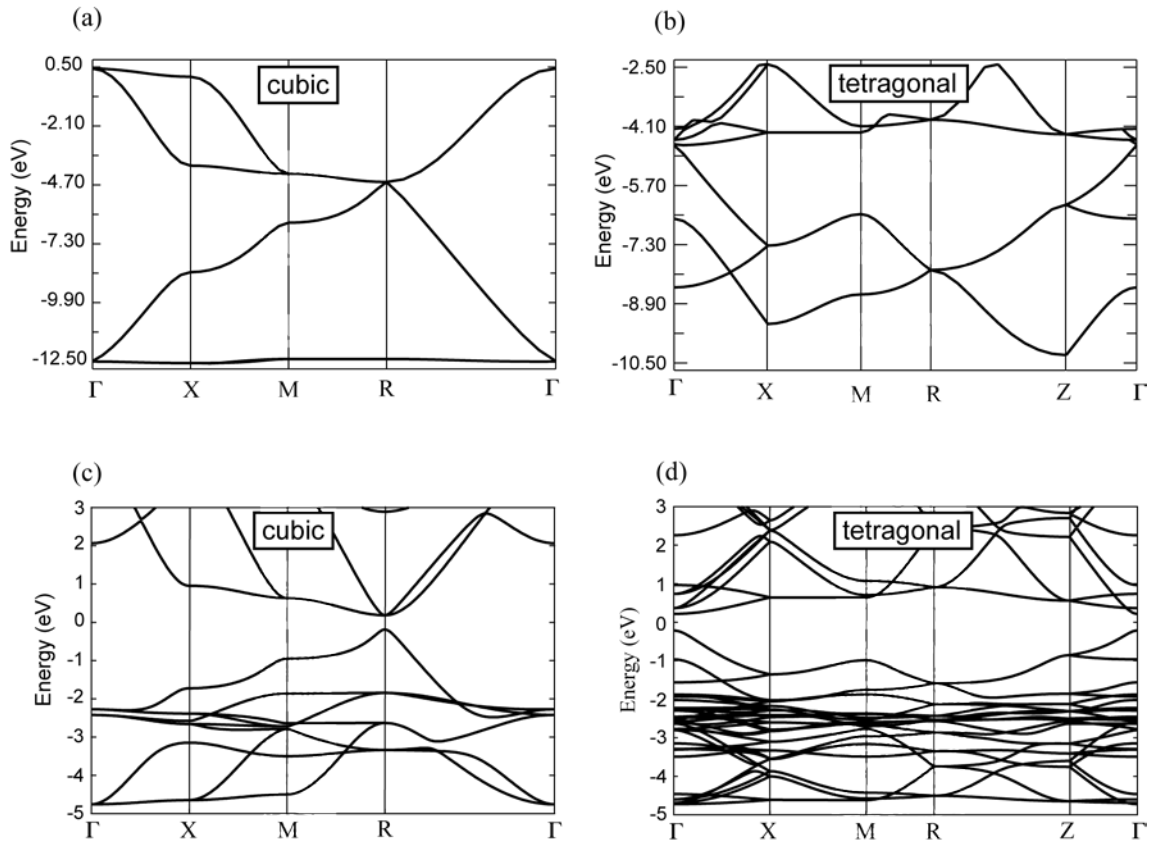


Fig. 2 Band structure obtained from extended Hückel calculations (a, b) and first-principles calculations (c, d) of $\text{CH}_3\text{NH}_3\text{SnI}_3$. For (a) and (b), CH_3NH_3 is not

included in the calculations, while for (c) and (d), Cs is placed at the A-site instead of CH_3NH_3 to mimic the cubic or tetragonal symmetry. Dispersion diagrams of (a) and (c) are the cubic phase, and those of (b) and (d) are the tetragonal phase.

With lowering of the temperature, the cubic structure transforms into a tetragonal structure. Upon this transition, the width of the valence band does not change much (Figs. 2b, d). On the other hand, the gap energy is increased to 0.43 eV in the first-principles calculation (Fig. 2d; the direct gap is moved to the Γ point due to change of the lattice system from P to I).

Charge transport

The temperature dependence of the single-crystal resistivity is shown in Fig. 3. The behavior is metallic for the crystals obtained from HI (method B) and ethanol (method C); the resistivity decreases with decreasing temperature over the measured temperature range. The temperature dependence of the pressed-powder resistivity was also metallic over a wide temperature range.¹ However, its parabolic dependence is more clear in the single-crystal measurements. The resistivity change with temperature is much larger in the present measurements ($\rho(300\text{ K})/\rho(10\text{ K}) \approx 50$) compared to the powder measurements ($\rho(300\text{ K})/\rho(10\text{ K}) \approx 3$). Furthermore, the phase transitions can be clearly seen: for the lower temperature transition, a resistivity jump with a hysteresis loop of 108–114 K occurs. The resistivity responds to these structural transitions, whereas the temperature dependence is metallic in all the phases. This means that the transport mechanism is relatively insensitive to the structural transitions. If the cubic phase had a

semi-metal electronic structure, a serious effect on the resistivity would be expected at the transition to the tetragonal phase due to the shifts of the top of the valence band and the bottom of the conduction band that induce changes in the number of charge carriers. However, only an insignificant change in the resistivity was observed at this transition. This fact suggests an electronic structure in which only doped holes in the top of the valence band respond to charge transport in this material.

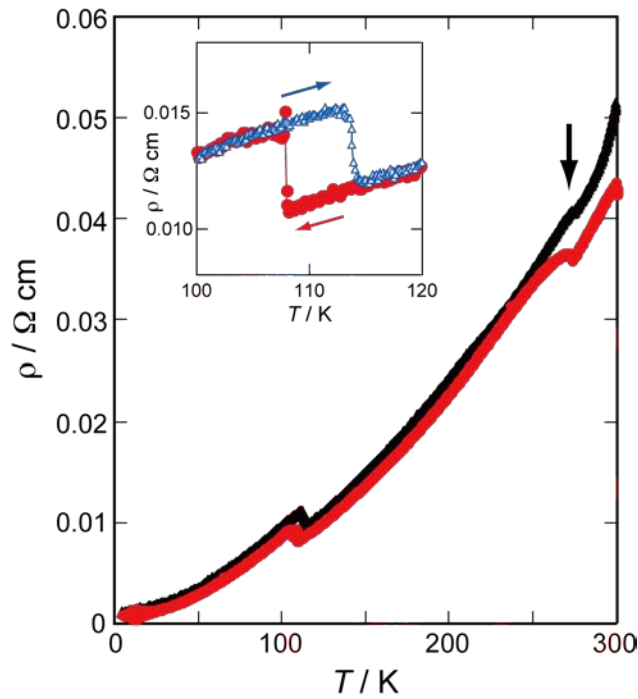


Fig. 3 Temperature dependence of the electrical resistivity of single-crystal $\text{CH}_3\text{NH}_3\text{SnI}_3$ grown from the HI solution (black) and that grown from the EtOH solution (red). The black arrow indicates a kink corresponding to the cubic-tetragonal phase transition. **Inset:** Close-up of the resistivity change at the phase transition near 110 K (red: decreasing temperature, blue: increasing temperature).

Fig. 4 shows the temperature dependence of the thermoelectric power (S). Although the behavior in the high-temperature region is not clear, the overall dependence almost

linearly correlates with the temperature, which is consistent with the metallic conductivity. Although there is a small discontinuity at the phase transition around 110 K, the slope does not change in both phases above and below this anomaly. The sign of S is positive over the whole temperature range, indicating that the carriers are holes. The temperature dependence is definitely metallic, but its rather large value should be noted. Because the thermoelectric power of ordinary metals is generally less than $10 \mu\text{V deg}^{-1}$ at room temperature, the value found in $\text{CH}_3\text{NH}_3\text{SnI}_3$ can be considered unusually large, which is obviously inappropriate for a semi-metal. The thermoelectric power of metallic conductors²⁸ is described as

$$S(T) = (\pi^2 k^2 T / 3e) [\delta \ln \sigma(E) / \delta E]_{E=E_F} \quad (1),$$

where k is the Boltzmann constant, e is the unit charge of the carrier, E_F is the Fermi energy, and σ is the conductivity. The equation can be rewritten as

$$S(T) = (\pi^2 k^2 T / 3e) (1/E_F) [\delta \ln \sigma(E) / \delta \ln E]_{E=E_F} \quad (2),$$

because $[\delta \ln \sigma(E) / \delta \ln E]_{E=E_F}$ for a simple metal usually becomes a constant, the value of which varies according to the band structure (neglecting the relaxation time). For example, it becomes 1/2 for a three-dimensional free-electron model. Thus, a large slope of $S(T)$ yields an extremely small E_F for holes with a value of only 0.03 eV. This indicates that only a small number of holes in a narrow range at the top of the valence band contribute to charge transport. The concentration of holes can be estimated from the density of states in the band calculation of the tetragonal phase. The concentration is $2.6 \times 10^{22} \text{ m}^{-3}$, corresponding to 0.0006 % of the doping level. Therefore, thermoelectric power measurements also suggest that this material is a semiconductor

modified by low levels of hole doping rather than a semi-metal. Because the width of the valence band is rather large, about 5 eV, mobility is considered to be high. This situation may be responsible for the diffusive character of the holes even at low concentrations, leading to the metallic charge transport.

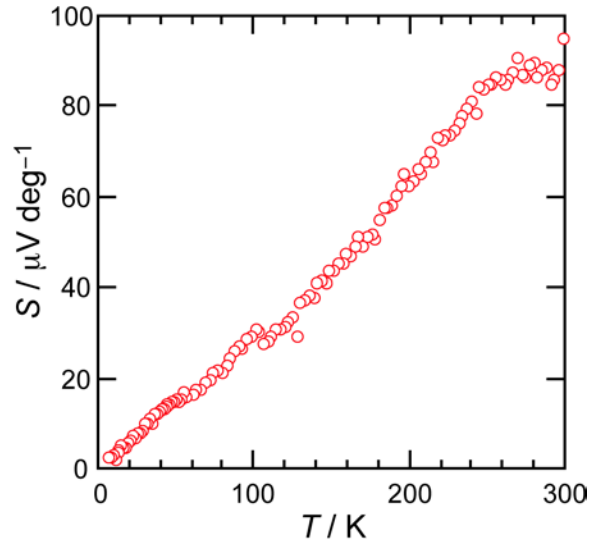


Fig. 4 Temperature dependence of the thermoelectric power (S) of single-crystal $\text{CH}_3\text{NH}_3\text{SnI}_3$.

Artificial hole doping

To verify the semiconducting electronic structure in $\text{CH}_3\text{NH}_3\text{SnI}_3$, artificial hole doping was performed. Because the main components of the top of the valence band are occupied Sn 5s and I 5p orbitals, holes may be distributed as electron deficient SnI_6 octahedral sites. To increase the number of such sites, partial replacement of tin(II) with tin(IV) is considered to be effective. Therefore, a part of the SnI_2 in the crystal growth solution of method C was replaced with SnI_4 . The temperature dependence of the resistivity of the artificially doped crystal thus obtained is shown in Fig. 5a. The resistivity over the whole temperature range decreases by the doping of SnI_4 . This

parallel shift of the resistivity indicates that the number of carriers is increased by incorporation of SnI_4 , whereas the temperature dependence of the mobility is not affected.

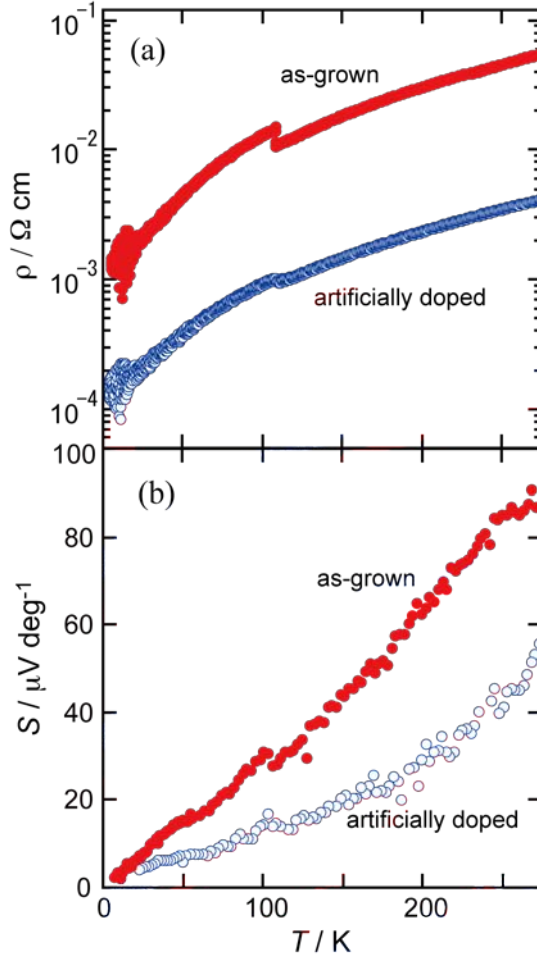


Fig. 5 Change in the (a) electrical resistivity and (b) thermoelectric power caused by artificial doping.

The temperature dependence of the thermoelectric power of the artificially doped crystal is shown in Fig. 5b. The slope of S is decreased in the artificially doped crystal. From the slope for the doped crystal, E_F is estimated to be about 0.05 eV. This value indicates that the number of carriers (holes) is increased by incorporation of SnI_4 . From

the density of states obtained from the band calculation, the concentration of holes is estimated to be $1.2 \times 10^{23} \text{ m}^{-3}$ from E_F , corresponding to the doping level of 0.003 %. It should be noted that the doping level even in the artificially doped crystal is still very small, although the number of carriers is increased from the as-grown crystal. In any case, successive change in the transport properties by artificial doping strongly supports the suggestion that the as-grown $\text{CH}_3\text{NH}_3\text{SnI}_3$ is a doped semiconductor. Because the hole doping inevitably accompanies charge defects at the CH_3NH_3 sites (deprotonation or cation defect) for charge neutrality, we need to control the charge defect at the same time to enhance the doping level.

Conclusions

By summarizing and analyzing all the results of band calculations and charge transport measurements of as-grown and artificially doped $\text{CH}_3\text{NH}_3\text{SnI}_3$, the metallic charge transport in the as-grown crystal is considered to result from low levels of spontaneous hole doping.

The interpretation of the electronic properties of $\text{CH}_3\text{NH}_3\text{SnI}_3$ in the present study is exactly the same as that recently proposed for the A_2SnI_4 layered-perovskites.⁷ In this layered system, an increase in the conductivity was actually observed upon doping of Sn^{IV} . The concentration of the acceptor sites was, however, still less than 1%, and metallic transport was not achieved. In both cubic and layered tin-iodide perovskite systems, spontaneous hole doping may inevitably occur in the crystal growth process. In $\text{CH}_3\text{NH}_3\text{SnI}_3$, because the conduction path is three-dimensional and the valence band is

sufficiently wide, delocalization of the doped holes, which leads to metallic transport, can easily be achieved.

Acknowledgements

This work was supported in part by a Grant-in-Aid for Scientific Research (22350055) and a Grant-in-Aid for JSPS fellows from Japan Society for the Promotion of Science, and by the GCOE program (Project No. B01: Catalysis as the Basis for Innovation in Materials Science) from the Ministry of Education, Culture, Sports, Science and Technology, Japan, and by JST, CREST. The authors thank Profs. Y. Hinatsu and R. Wakeshima at Hokkaido Univ. for their help in the powder diffraction measurements.

References

- 1 D. B. Mitzi, C. A. Feild, Z. Schlesinger and R. B. Laibowitz, *J. Solid State Chem.*, 1995, **114**, 159-163.
- 2 I. Borriello, G. Cantele and D. Ninno, *Phys. Rev. B*, 2008, **77**, 235214.
- 3 F. Chiarella, A. Zappettini and F. Licci, *Phys. Rev. B*, 2008, **77**, 045129.
- 4 D. B. Mitzi and K. Liang, *J. Solid State Chem.*, 1997, **134**, 376-381.
- 5 D. B. Mitzi, C. A. Feild, W. T. A. Harrison and A. M. Guloy, *Nature*, 1994, **369**, 467-469.
- 6 D. B. Mitzi, S. Wang, C. A. Feild, C. A. Chess and A. M. Guloy, *Science*, 1995, **267**, 1473-1476.
- 7 Y. Takahashi, R. Obara, K. Nakagawa, M. Nakano, J. Tokita and T. Inabe, *Chem. Mater.*, 2007, **19**, 6312-6316.
- 8 D. B. Mitzi, *Prog. Inorg. Chem.*, 1999, **48**, 1-121.
- 9 D. B. Mitzi, *J. Chem. Soc., Dalton Trans.*, 2001, 1-12.
- 10 G. C. Papavassiliou, *Prog. Solid St. Chem.*, 1997, **25**, 125-270.
- 11 G. C. Papavassiliou and I. B. Koutselas, *Synth. Met.*, 1995, **71**, 1713-1714.
- 12 J. L. Knutson, J. D. Martin and D. B. Mitzi, *Inorg. Chem.*, 2005, **44**, 4699-4705.
- 13 D. B. Mitzi, *Chem. Mater.*, 1996, **8**, 791-800.
- 14 R. W. Schaeffer, B. Chan, M. Molinaro, S. Morissey, C. H. Yoder, C. S. Yoder and S. Shenk, *J. Chem. Educ.*, 1997, **74**, 575-577.
- 15 SIR92: A. Altomare, M. C. Burla, M. Camalli, M. Cascarano, C. Giacovazzo, A. Guagliardi and G. Polidori, *J. Appl. Cryst.*, 1994, **27**, 435.

- 16 CrystalStructure 3.5.1: Crystal Structure Analysis Package, Rigaku and Rigaku/MSK (2000-2003). 9009 New Trails Dr. The Woodlands TX 77381 USA, b) CRYSTALS Issue 10: D. J. Watkin, C. K. Prout, J. R. Carruthers and P.W. Betteridge, Chemical Crystallography Laboratory, Oxford, UK (1996).
- 17 P. M. Chaikin and J. F. Kwak, *Rev. Sci. Instrum.*, 1975, **46**, 429.
- 18 J. Ren, W. Liang and M.-H. Whangbo, *Crystal and Electronic Structure Analysis Using CAESER*, PrimeColor Software, Inc., Cary, North Carolina, U.S.A., (1998).
- 19 S. Ishibashi, T. Tamura, S. Tanaka, M. Kohyama and K. Terakura, <http://qmas.jp>.
- 20 P. E. Blöchl, *Phys. Rev. B*, 1994, **50**, 17953.
- 21 J. P. Perdew, K. Burke and M. Ernzerhof, *Phys. Rev. Lett.*, 1996, **77**, 3865.
- 22 Q. Xu, T. Eguchi, H. Nakayama, N. Nakamura and M. Z. Kishida, *Naturforsch. A*, 1990, **46**, 240.
- 23 Y. Kawamura, H. Mashiyama and K. Hasebe, *J. Phys. Soc. Jpn.*, 2002, **71**, 1694-1697.
- 24 A. M. Glazer, *Acta Crystallogr.*, 1972, **B28**, 3384-3392.
- 25 A. Poglitsch and D. Weber, *J. Chem. Phys.*, 1987, **87**, 6373-6378.
- 26 I. B. Koutselas, L. Ducasse and G. C. Papavassiliou, *J. Phys.: Condens. Matter*, 1996, **8**, 1217-1227.
- 27 J.-F. Chabot, M. Côté and J.-F. Brière, High Performance Computing Systems and Applications and OSCAR Symposium (Proceedings), D. Senechal (Ed.), NRC Research Press, Ottawa, 2003; <http://hpcs2003.ccs.usherbrooke.ca/program.html>.
- 28 J. M. Ziman, Principles of the theory of solids, 2nd ed., Chapt. 7, Cambridge Univ.

Press, Cambridge, 1972.

Graphical contents entry:

Charge-Transport in Tin-Iodide Perovskite $\text{CH}_3\text{NH}_3\text{SnI}_3$: Origin of High Conductivity

Yukari Takahashi, Rena Obara, Zheng-Zhong Lin, Yukihiro Takahashi, Toshio Naito, Tamotsu Inabe, Shoji Ishibashi and Kiyoyuki Terakura

Single crystal tin-iodide perovskite, $\text{CH}_3\text{NH}_3\text{SnI}_3$, shows metallic electrical conductivity despite a well-defined band gap at the Fermi level, and is suggested to be a doped semiconductor.

